The Astrophysical Journal, 767:132 (11pp), 2013 April 20 doi:10.1088/0004-637X/767/2/132

ALMA OBSERVATIONS OF SPT-DISCOVERED, STRONGLY LENSED, DUSTY, STAR-FORMING GALAXIES

Y. D. Hezaveh[1], D. P. Marrone[2], C. D. Fassnacht[3], J. S. Spilker[2], J. D. Vieira[4], J. E. Aguirre[5], K. A. Aird[6], M. Aravena[7], M. L. N. Ashby[8], M. Bayliss[8,9], B. A. Benson[10,11], L. E. Bleem[10,12], M. Bothwell[2], M. Brodwin[13], J. E. Carlstrom[10,11,12,14,15], C. L. Chang[10,11,15], S. C. Chapman[16,17], T. M. Crawford[10,14], A. T. Crites[10,14], C. De Breuck[7], T. de Haan[1], M. A. Dobbs[1], E. B. Fomalont[18], E. M. George[19], M. D. Gladders[10,14], A. H. Gonzalez[20], T. R. Greve[21], N. W. Halverson[22], F. W. High[10,14], G. P. Holder[1], W. L. Holzapfel[19], S. Hoover[10,11], J. D. Hrubes[6], K. Husband[17], T. R. Hunter[18], R. Keisler[10,12], A. T. Lee[19,23], E. M. Leitch[10,14], M. Lueker[4], D. Luong-Van[6], M. Malkan[24], V. McIntyre[25], J. J. McMahon[10,11,26], J. Mehl[10,14], K. M. Menten[27], S. S. Meyer[10,11,12,14], L. M. Mocanu[10,14], E. J. Murphy[28], T. Natoli[10,12], S. Padin[4,10,14], T. Plagge[10,14], C. L. Reichardt[19], A. Rest[29], J. Ruel[9], J. E. Ruhl[30], K. Sharon[10,14,31], K. K. Schaffer[10,32], L. Shaw[1,33], E. Shirokoff[4], B. Stalder[8], Z. Staniszewski[4,30], A. A. Stark[8], K. Story[10,12], K. Vanderlinde[1], A. Weiß[27], N. Welikala[34], and R. Williamson[10,14]

[1] Department of Physics, McGill University, 3600 Rue University, Montreal, Quebec H3A 2T8, Canada
[2] Steward Observatory, University of Arizona, 933 North Cherry Avenue, Tucson, AZ 85721, USA
[3] Department of Physics, University of California, One Shields Avenue, Davis, CA 95616, USA
[4] California Institute of Technology, 1200 E. California Blvd., Pasadena, CA 91125, USA
[5] University of Pennsylvania, 209 South 33rd Street, Philadelphia, PA 19104, USA
[6] University of Chicago, 5640 South Ellis Avenue, Chicago, IL 60637, USA
[7] European Southern Observatory, Karl-Schwarzschild Strasse, D-85748 Garching bei München, Germany
[8] Harvard-Smithsonian Center for Astrophysics, 60 Garden Street, Cambridge, MA 02138, USA
[9] Department of Physics, Harvard University, 17 Oxford Street, Cambridge, MA 02138, USA
[10] Kavli Institute for Cosmological Physics, University of Chicago, 5640 South Ellis Avenue, Chicago, IL 60637, USA
[11] Enrico Fermi Institute, University of Chicago, 5640 South Ellis Avenue, Chicago, IL 60637, USA
[12] Department of Physics, University of Chicago, 5640 South Ellis Avenue, Chicago, IL 60637, USA
[13] Department of Physics and Astronomy, University of Missouri, 5110 Rockhill Road, Kansas City, MO 64110, USA
[14] Department of Astronomy and Astrophysics, University of Chicago, 5640 South Ellis Avenue, Chicago, IL 60637, USA
[15] Argonne National Laboratory, 9700 S. Cass Avenue, Argonne, IL, USA 60439, USA
[16] Department of Physics and Atmospheric Science, Dalhousie University, Halifax, NS B3H 3J5 Canada
[17] Institute of Astronomy, University of Cambridge, Madingley Road, Cambridge CB3 0HA, UK
[18] National Radio Astronomy Observatory, 520 Edgemont Road, Charlottesville, VA 22903, USA
[19] Department of Physics, University of California, Berkeley, CA 94720, USA
[20] Department of Astronomy, University of Florida, Gainesville, FL 32611, USA
[21] Department of Physics and Astronomy, University College London, Gower Street, London WC1E 6BT, UK
[22] Department of Astrophysical and Planetary Sciences and Department of Physics, University of Colorado, Boulder, CO 80309, USA
[23] Physics Division, Lawrence Berkeley National Laboratory, Berkeley, CA 94720, USA
[24] Department of Physics and Astronomy, University of California, Los Angeles, CA 90095-1547, USA
[25] Australia Telescope National Facility, CSIRO, Epping, NSW 1710, Australia
[26] Department of Physics, University of Michigan, 450 Church Street, Ann Arbor, MI, 48109, USA
[27] Max-Planck-Institut für Radioastronomie, Auf dem Hügel 69 D-53121 Bonn, Germany
[28] Observatories of the Carnegie Institution for Science, 813 Santa Barbara Street, Pasadena, CA 91101, USA
[29] Space Telescope Science Institute, 3700 San Martin Dr., Baltimore, MD 21218, USA
[30] Physics Department, Center for Education and Research in Cosmology and Astrophysics, Case Western Reserve University, Cleveland, OH 44106, USA
[31] Department of Astronomy, University of Michigan, 500 Church Street, Ann Arbor, MI, 48109, USA
[32] Liberal Arts Department, School of the Art Institute of Chicago, 112 S Michigan Ave, Chicago, IL 60603, USA
[33] Department of Physics, Yale University, P.O. Box 208210, New Haven, CT 06520-8120, USA
[34] Institut d'Astrophysique Spatiale, Bâtiment 121, Université Paris-Sud XI & CNRS, F-91405 Orsay Cedex, France
Received 2012 September 18; accepted 2013 March 1; published 2013 April 4

ABSTRACT

We present Atacama Large Millimeter/submillimeter Array (ALMA) 860 μm imaging of four high-redshift (z = 2.8–5.7) dusty sources that were detected using the South Pole Telescope (SPT) at 1.4 mm and are not seen in existing radio to far-infrared catalogs. At 1.″5 resolution, the ALMA data reveal multiple images of each submillimeter source, separated by 1″–3″, consistent with strong lensing by intervening galaxies visible in near-IR imaging of these sources. We describe a gravitational lens modeling procedure that operates on the measured visibilities and incorporates self-calibration-like antenna phase corrections as part of the model optimization, which we use to interpret the source structure. Lens models indicate that SPT0346-52, located at z = 5.7, is one of the most luminous and intensely star-forming sources in the universe with a lensing corrected FIR luminosity of $3.7 \times 10^{13}\ L_{\odot}$ and star formation surface density of 4200 $M_{\odot}$ yr^{-1} kpc^{-2}. We find magnification factors of 5 to 22, with lens Einstein radii of 1.″1–2.″0 and Einstein enclosed masses of 1.6–7.2 $\times 10^{11}\ M_{\odot}$. These observations confirm the lensing origin of these objects, allow us to measure their intrinsic sizes and luminosities, and demonstrate the important role that ALMA will play in the interpretation of lensed submillimeter sources.

Key words: galaxies: high-redshift – galaxies: starburst – gravitational lensing: strong – techniques: interferometric

Online-only material: color figures

1. INTRODUCTION

Half of the energy produced by all objects in the history of the universe has been absorbed and reemitted by dust (Dole et al. 2006). The Cosmic Infrared Background, first detected by the *Cosmic Background Explorer* satellite (Puget et al. 1996; Hauser et al. 1998; Fixsen et al. 1998), is the aggregate emission from individual dusty galaxies across cosmic time (e.g., Lagache et al. 2005). The brightest of these dusty star-forming galaxies (DSFGs) were discovered in deep submillimeter-wavelength images of the sky (Smail et al. 1997; Hughes et al. 1998; Barger et al. 1998), and have luminosities in excess of $10^{12}\ L_{\odot}$ emitted primarily at rest wavelength in the far-infrared. With star formation rates >100–1000 $M_{\odot}\ \mathrm{yr}^{-1}$, this population of DSFGs contributes a significant fraction of the total star formation density of the universe at $z \sim 2$–3, where their abundance peaks (e.g., Chapman et al. 2005). These objects are the progenitors of the massive galaxies we observe today.

Despite the enormous total luminosity of the brightest DSFGs, their detection at submillimeter wavelengths requires lengthy exposures for ground-based facilities, and they are generally quite dim at optical/NIR wavelengths due to extinction. Studies of these objects and their extreme star formation rates are limited by the observational costs of observing all but the brightest spectral lines and the poor spatial resolution achievable compared to the typical size of the star-forming regions. Gravitational lensing provides a solution to both of these problems, as has been demonstrated in a few spectacular cases (e.g., Kneib et al. 2004; Swinbank et al. 2010; Riechers et al. 2011; Fu et al. 2012). Lensed starburst galaxies can be examined at high spatial resolution and with a more diverse set of diagnostics than the unmagnified population (Swinbank et al. 2010).

Predictions of a large population of gravitationally lensed, high redshift DSFGs (Blain 1996; Negrello et al. 2007) were recently verified by large-area millimeter/submillimeter surveys (Vieira et al. 2010; Negrello et al. 2010; Wardlow et al. 2013). Hezaveh & Holder (2011) also predicted the number counts of bright lensed objects for mm-wavelength surveys using a detailed numerical method, with a proper treatment of finite source effects and lens ellipticities, confirming that realistic lens models were able to match the observed number counts of dusty sources reported in Vieira et al. (2010). These galaxies have a sky density of $\sim$0.1 deg^{-2}, and therefore can only be found in large numbers in extensive surveys. The South Pole Telescope (SPT; Carlstrom et al. 2011), which surveyed 2500 deg^2 to $\sim$ mJy depth at wavelengths of 3, 2, and 1.4 mm, has provided a sample of about one hundred candidate lensed sources (Vieira et al. 2010). Initial investigations of these objects have found them to have properties consistent with unlensed starbursts, except for their large apparent luminosities (Greve et al. 2012). Morphological evidence of lensing cannot be discerned in data from the SPT survey or the single-aperture followup of Greve et al. (2012), except in rare cases of lensing by clusters of galaxies, so arcsecond-resolution submillimeter imaging is required.

The Atacama Large Millimeter/submillimeter Array (ALMA; Hills et al. 2010) has begun operation in Chile, providing unprecedented submillimeter sensitivity even in early science. In this work, we employ ALMA to measure the arcsecond-scale structure of dusty extragalactic SPT sources at millimeter wavelengths, confirming the lensed nature of the four sources presented here. The observations reported here represent <10% of our Cycle 0 sample and use only the compact configuration data, which was delivered first. Nevertheless, from these ALMA data, we are able to model the lensing geometry of these sources and de-magnify them, allowing them to be placed in the proper context within the high-redshift galaxy population. We are also able to infer the total mass and ellipticity of the lenses, a first step toward using the lensed submillimeter emission to characterize the lensing potential and its substructure. In Section 2, we describe the ALMA observations and supporting data, and in Section 3 we describe a modeling technique for interferometric measurements of gravitationally lensed sources. Additional details on the integrated self-calibration step are included in the Appendix. In Section 4, we discuss the properties of the sources and lenses and present the conclusions in Section 5. Throughout this work, we assume a ΛCDM cosmology, with WMAP7 parameters, with $h = 0.71$, $\Omega_M = 0.27$, and $\Omega_\Lambda = 0.73$ (Komatsu et al. 2011).

2. OBSERVATIONS

2.1. ALMA Imaging

The primary observations for this work were obtained from ALMA under a Cycle 0 program (2011.0.00958.S; PI: D. Marrone) in which 47 sources identified in the SPT survey are each observed in both the compact and extended array configurations. The first data release for this program includes 20 sources observed in the compact array configuration; here, we focus on the four sources for which these low-resolution data were sufficient to resolve the targets into multiple components. Of the remaining 16 sources, at least 8 are not point-like at the resolution of these observations, but we defer lens modeling for these sources until the remaining data are in hand.

The sources were targeted for brief snapshot observations with the dual-polarization Band 7 (275–373 GHz) receivers on two dates, 2011 November 16 and 28. The first local oscillator was set to 343.8 GHz, with all four spectral windows configured in time domain mode with 128 channels of 15.625 MHz width centered at 5.125 and 7 GHz IF in each sideband. There were 16 and 14 antennas available on these days, respectively, arranged in a compact configuration. The total elapsed time (for all sources, including those not published here) in the observations was approximately 4.1 hr. The total integration time per source was 61 and 91 s in the first and second tracks, respectively, with 6.1-s sampling of the visibility data. The array alternately observed the science targets and gain calibrators (30 s), observing the calibrator every three to four minutes. Additional sources with known positions, precisely established against the International Celestial Reference Frame using very long baseline interferometry (Ma et al. 1998), were added to the tracks to verify astrometry and calibration and observed with the same cycle as the science targets.

The flux scale was set with observations of Callisto on the first day. On the second day, the flux scale was derived by setting the flux of quasar J0403-360 to 1.84 Jy, as reported by the ALMA staff from adjacent calibration observations. The absolute flux density scale is correct to within 15%. The antenna gains are equalized through gain calibration (amplitude and phase) on the main calibrators in each track. Short-timescale phase correction is achieved using the ALMA water vapor radiometry (WVR) system. Very little variation is observed in these gain amplitudes through the tracks, and there is no evidence for atmospheric decorrelation on the longest baselines in the phase scatter of the target or calibrator visibilities after WVR phase correction. The data were processed with the Common Astronomy Software

Table 1
Source and Lens Parameters

							Source Intrinsic Properties				
ID	z_S	z_L	r_E	M_L	ϵ_L	μ	$R_{1/2}$	L_{FIR}	Σ_{FIR}	$S_{1.4mm}$	$S_{860\mu m}$
(1)	(2)	(3)	(4)	(5)	(6)	(7)	(8)	(9)	(10)	(11)	(12)
SPT-S J034640−5205.1	5.656	...	1.124 ± 0.004	3.73 ± 0.04[a]	0.55 ± 0.01	5.4 ± 0.2	0.59 ± 0.03	37.3 ± 2.8	24	8.1	23.0
SPT-S J041840−4752.0	4.224	0.265	1.390 ± 0.012	2.39 ± 0.04	0.20 ± 0.03	21.0 ± 3.5	1.07 ± 0.17	3.8 ± 0.7	0.74	1.6	5.0
SPT-S J052903−5436.6	3.369	0.140	1.536 ± 0.017	1.64 ± 0.04	0.10 ± 0.03	9.4 ± 1.0	2.39 ± 0.24	3.8 ± 0.5	0.15	3.8	15.6
SPT-S J053816−5030.8	2.782	0.404	1.987 ± 0.009	7.15 ± 0.05	0.13 ± 0.02	20.5 ± 4.0[b]	...	4.5 ± 0.9	...	1.5	5.8
SPT0538-50 A						19.8 ± 4.6	0.52 ± 0.12	3.0[c]	2.4[c]		
SPT0538-50 B						21.9 ± 3.7	1.61 ± 0.33	1.4[c]	0.12[c]		

Notes. Column 1: SPT source name. Column 2: background source redshift. Column 3: lens redshift. Column 4: Einstein radius (arcsec). Column 5: lens mass, interior to r_E (10^{11} $M_\odot$). Column 6: lens ellipticity. Column 7: total magnification of background source. Column 8: source radius, determined as the half-width at half-maximum for the Gaussian source component in the model fit (kpc). Column 9: intrinsic far infrared luminosity (10^{12} $L_\odot$). Column 10: intrinsic source flux (luminosity per area; 10^{12} $L_\odot$/kpc^2). Column 11: intrinsic 1.4 mm flux density, obtained as the SPT flux density divided by μ (mJy). Column 12: the same as (11), but for the ALMA 350 GHz (860 μm) flux density. The parameter uncertainties do not include a contribution from the cosmological parameters. An additional 4% uncertainty in mass is found by marginalizing over the WMAP7 parameter Markov chains.

[a] Assuming that the lens is located at $z = 0.8$, see Section 4.

[b] Total magnification of the two source components, see Section 4.

[c] Derived assuming that L_{FIR} is divided between components in the same ratio as the flux density in the model.

Applications package (McMullin et al. 2007; Petry et al. 2012) using standard steps for a continuum observation.

The four well-resolved sources are listed in Table 1, and we refer to them throughout the paper with shortened versions of their coordinate-based names (e.g., SPT0346-52 for SPT-S J034640−5205.1). Observations on November 16 included baselines of 15–150 kλ, resulting in synthesized beams of $1\farcs5 \times 1\farcs3$ (FWHM) for the RA = 5^h sources. The uv coverage on November 28 was less uniform and spanned 15–240 kλ, providing a synthesized beam of $2\farcs1 \times 0\farcs9$ for the other two sources. Deconvolved source images and beam shapes are shown in Figure 1.

2.2. Redshift Determinations

Table 1 shows source and lens redshifts, as available, for these four SPT sources. Redshifts for three of the dusty sources were obtained in another ALMA Cycle 0 project (2011.0.00957.S; PI: A. Weiss) through a spectral line survey conducted using the Band 3 (84–116 GHz) receivers. The complete results of this survey will be reported in Vieira et al. (2013) and Weiß et al. (2013). For each of these sources, multiple high-significance lines are detected in the Band 3 spectral scan, providing unambiguous redshifts. In the case of SPT0538-50, a redshift was determined from a combination of millimeter-wavelength and optical spectroscopy, as described in Greve et al. (2012), and the source was not included in the ALMA redshift search proposal.

The combination of NIR pre-imaging and submillimeter interferometric observations described below provided the basis for ground-based spectroscopic observations of the putative lens galaxies. The fields of SPT0346-52, SPT0418-47, and SPT0529-54 were targeted first with *R*-band pre-imaging, then with multi-object masks, using the Mask Exchange Unit of FORS2 (Appenzeller et al. 1998) on the Very Large Telescope (VLT) UT1, and exposing them for 3 × 900 s integrations each. The data were collected during 2012 February and March, in Service Mode (ESO program ID 088.A-0902) under an average seeing of $\sim 1\farcs1$. The galaxies were observed with slits of $1''$ in width using the G300 V grism, yielding a velocity resolution of $\sim$650 km s^{-1} or $\sim$13 Å, sampled at $\sim$3.3 Å pixel^{-1}. SPT0538-50 was observed with the XSHOOTER echelle spectrograph (Vernet et al. 2011) in longslit mode. For these observations, the slit widths were $1''$ (UV-B), $0\farcs9$ (VIS-R), and $0\farcs9$ (NIR); the corresponding resolving powers are $R = 5100$, 8800, and 5600, sampled with 3.2, 3.0, and 4.0 wavelength bins, respectively (after on-chip binning by a factor of two of the UV-B and VIS-R detectors). 6 × 900 s integrations were obtained in 2010 February, however, half of these were taken under worse conditions and we use only the better three integrations in the spectrum presented here.

The observations were prepared and the data reduced using the standard ESO pipeline,[35] performing bias and flat corrections, background subtraction, fringe correction, registration and combination, wavelength calibration, and one-dimensional spectral extractions. Spectra are shown in Figure 2. With the exception of SPT0346-52, redshifts for the lensing galaxies were measured by fitting Gaussians to the Ca K+H absorption lines.

2.3. Other Supporting Data

The small primary beam size of the 12 m ALMA antennas at 350 GHz required that we improve upon the $\sim 10''$ positional uncertainty of the SPT detections before proposing ALMA observations. These targets were initially followed up with the Submillimeter Array (SMA; Blundell 2004; Ho et al. 2004), or the Australia Telescope Compact Array[36] (ATCA; SPT0529-54 only). The SMA observations (M. Bothwell et al., in preparation) had a typical angular resolution of $3'' \times 12''$ because of the low declination of the sources, but those data gave some indication that the submillimeter emission was resolved. The 100 GHz ATCA detection of SPT0529-54 was of low significance and did not reveal any ringlike structure.

Deep near-infrared (NIR) imaging data were acquired from the Southern Astrophysical Research (SOAR) Telescope (OSIRIS; Depoy et al. 1993), the Very Large Telescope (VLT ISAAC; Moorwood et al. 1998), and the *Hubble Space Telescope* (*HST*), as part of followup programs to examine lens properties and identify rest-frame optical emission from the background sources.

[35] http://www.eso.org/sci/facilities/paranal/instruments/fors—VLT-MAN-ESO-19500-1771

[36] http://www.narrabri.atnf.csiro.au/

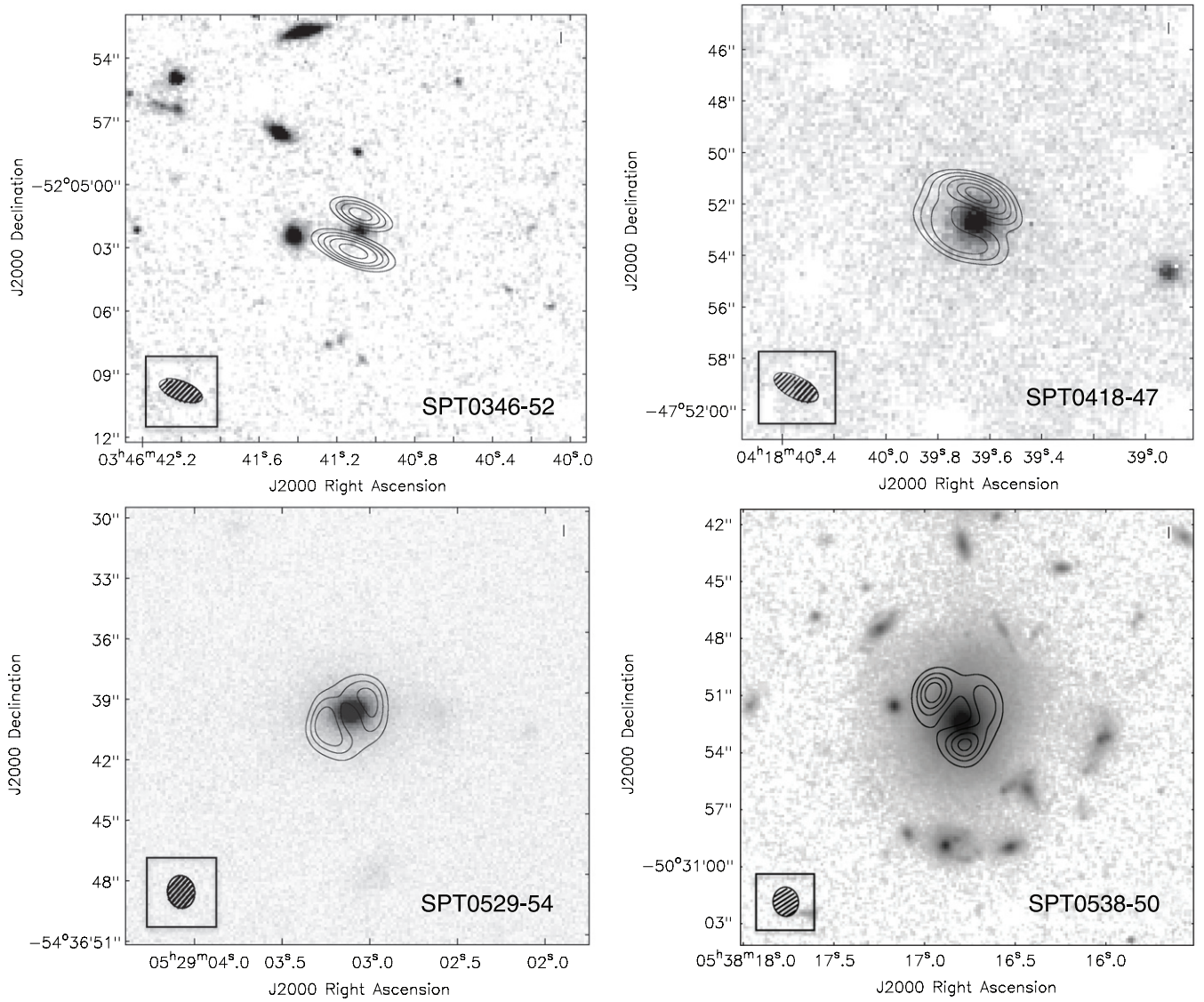

Figure 1. ALMA 350 GHz CLEANed images of the lensed DSFGs (contours), on top of NIR imaging of the galaxy field (grayscale) from *Hubble Space Telescope*, VLT, and SOAR. From left to right, they are SPT0346-52 (*HST*) and SPT0418-47 (VLT) in the top row and SPT0529-54 (SOAR) and SPT0538-50 (*HST*) in the bottom row. The ALMA contours begin at 5σ, increasing in steps of 10σ in the top left and bottom right images, and 5σ in the other two, as in Figure 4. The synthesized beam is shown in the lower left of each image. The *HST* images are a composite of the F110W and F160W filters, the VLT images are *K* band from ISAAC, and the SOAR image is *K* band from OSIRIS.

The luminosities in Table 1 are derived from photometric observations at millimeter to submillimeter wavelengths. In addition to SPT photometry (1.4 and 2 mm), we use 870 μm observations from LABOCA (Siringo et al. 2009) on the APEX telescope (in Max Planck time) and *Herschel*-SPIRE photometry at 250, 350, and 500 μm. The LABOCA data were analyzed according to the procedure described in Greve et al. (2012). The *Herschel* data are reduced as described in Weiß et al. (2013). All photometric data, including SPT measurements and the data previously reported in Greve et al. (2012) for SPT0529-54 and SPT0538-50, are provided in Weiß et al. (2013). The LABOCA measurements of the total 870 μm flux density agree with the total flux density in the modeled ALMA data (described below) to within calibration uncertainties, typically 10%. Luminosities are calculated using a graybody model like that described in Greve et al. (2012), though in the present case, the $\tau = 1$ wavelength is a parameter of the fit. The effect of freeing this parameter is to broaden the peak of the spectral energy distribution (SED) as needed to match the short-wavelength *Herschel* data points.

3. RESULTS AND ANALYSIS

Figure 1 presents the resolved structure of the 350 GHz emission associated with the SPT sources, as revealed in Cycle 0 ALMA observations, and the NIR emission at the same positions. In all cases, there is a clear NIR counterpart to the submillimeter source, though with no structural correspondence between the infrared sources and the emission found in the ALMA images. The morphologies of these sources at submillimeter wavelengths are indicative of gravitational lensing. The redshift identifications reported in Table 1, with very high redshifts measured for the dusty emission behind low-redshift foreground galaxies, clearly confirm these systems as galaxy–galaxy lenses. A similar finding was reported in Negrello et al. (2010), where bright sources selected at much shorter wavelength from

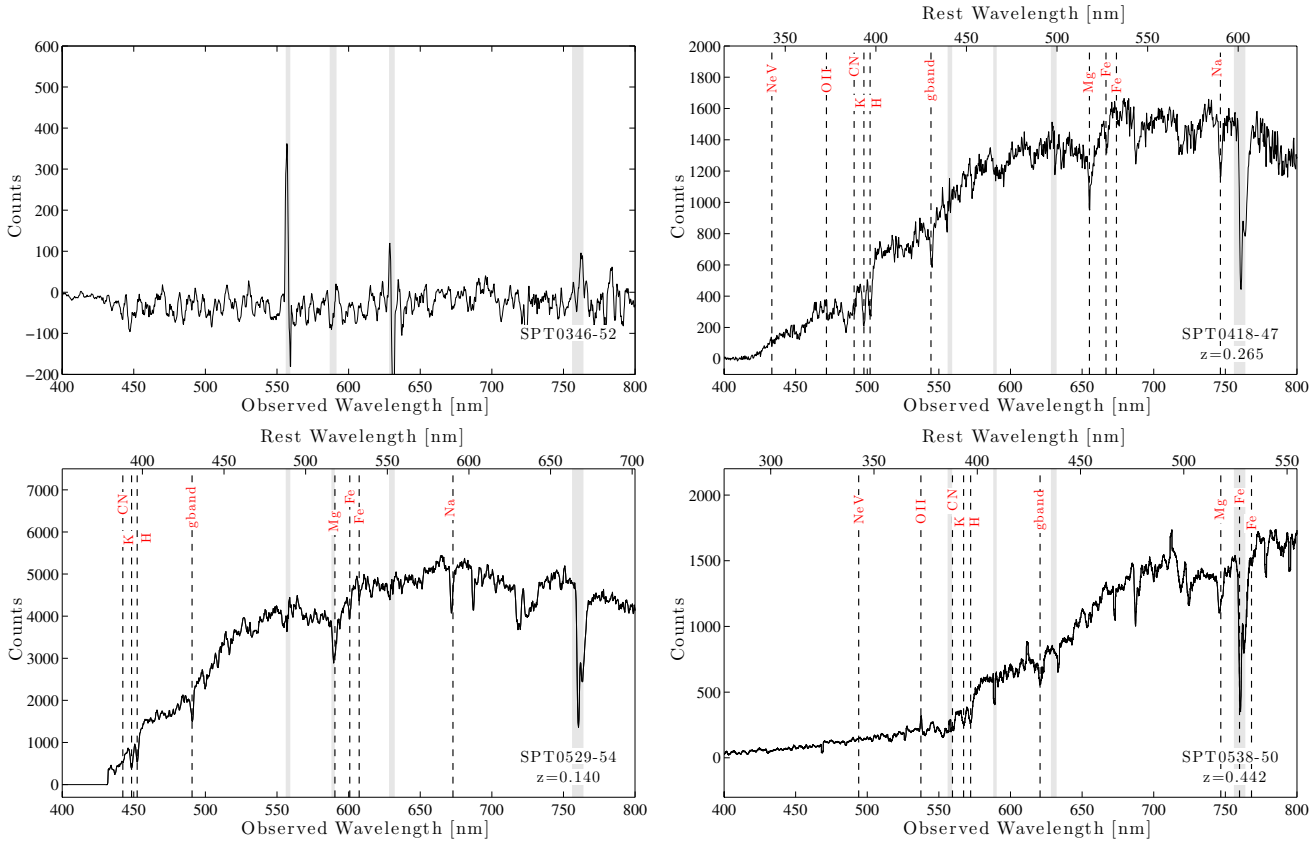

Figure 2. Optical spectra of the foreground lenses, from the VLT. The positions of major lines are marked by thin dashed lines. Sky lines are marked with gray shaded regions.

(A color version of this figure is available in the online journal.)

wide-field submillimeter surveys with *Herschel*-SPIRE were also confirmed to be gravitationally lensed.

3.1. Lens Modeling

The ALMA interferometer measures visibilities, Fourier components of the sky intensity distribution across a two-dimensional range of spatial frequencies, rather than directly imaging the emission. To properly compare these data with a source model, we must perform our analysis in the visibility plane, where the measurement and its noise are well understood (e.g., Bussman et al. 2012). Past techniques for modeling interferometric lens observations (e.g., Wucknitz et al. 2004) have generally operated on reconstructed images that are subject to difficult-to-model biases and noise properties. Furthermore, residual errors in calibration in the visibility data, such as those arising from imperfect knowledge of the antenna positions or uncompensated atmospheric delay, are often corrected as part of the imaging process through an iterative clean/self-calibration technique (Cornwell et al. 1999). However, the inclusion of the cleaning step in the determination of these corrections, which are then applied to the visibility data themselves, changes the data in ways that are not easily included in the modeling uncertainties. Here, we describe a visibility-based lens modeling technique that simultaneously determines these self-calibration phases so that we incorporate the full range of uncertainty present in the measurements.

We model the lenses by generating model lensed images that are subjected to simulated observations and compared to the data. The source is assumed to have a symmetric Gaussian light profile with four free parameters: flux density F_S, radius R_S, and positional offsets from the lens center X_S, Y_S. The lens is modeled as a Singular Isothermal Ellipsoid (SIE) with five free parameters: mass inside the Einstein radius M_L, ellipticity ϵ_L, orientation angle θ_L (east of north), and position X_L, Y_L. The SIE profile has been shown to be a good approximation to galaxy-scale density profiles (Treu & Koopmans 2004; Koopmans et al. 2006, 2009). Since lensed image positions provide very precise measurements of the projected mass interior to the images, we report this robustly measured quantity in Table 1, the total mass (M_L) inside the Einstein radius (r_E) of the lensing galaxies. However, the total halo masses associated with these galaxies will be much higher. Magnification, μ, is calculated as the ratio of the total lensed to unlensed flux.

Given a set of lens and source parameters, we make a high-resolution image of the lensed source, which we pad with zeroes and Fourier transform to generate model visibilities. For each ALMA visibility, we interpolate the Fourier transformed image to the ALMA u, v coordinates. We also correct for the antenna primary beam attenuation by multiplying the sky model images by the primary beam pattern before sampling the Fourier modes. We use a symmetric Gaussian with FWHM of 18″ for the primary beam, which leads to minimal attenuation for these well-centered sources.

The agreement between data and model visibilities is determined by calculating the χ^2 between them, which requires an estimate of the visibility noise. Because we observe strong sources, the visibility scatter has a contribution from the sky signal and cannot be used to determine the noise level. Instead, we derive noise levels by measuring visibility scatter after

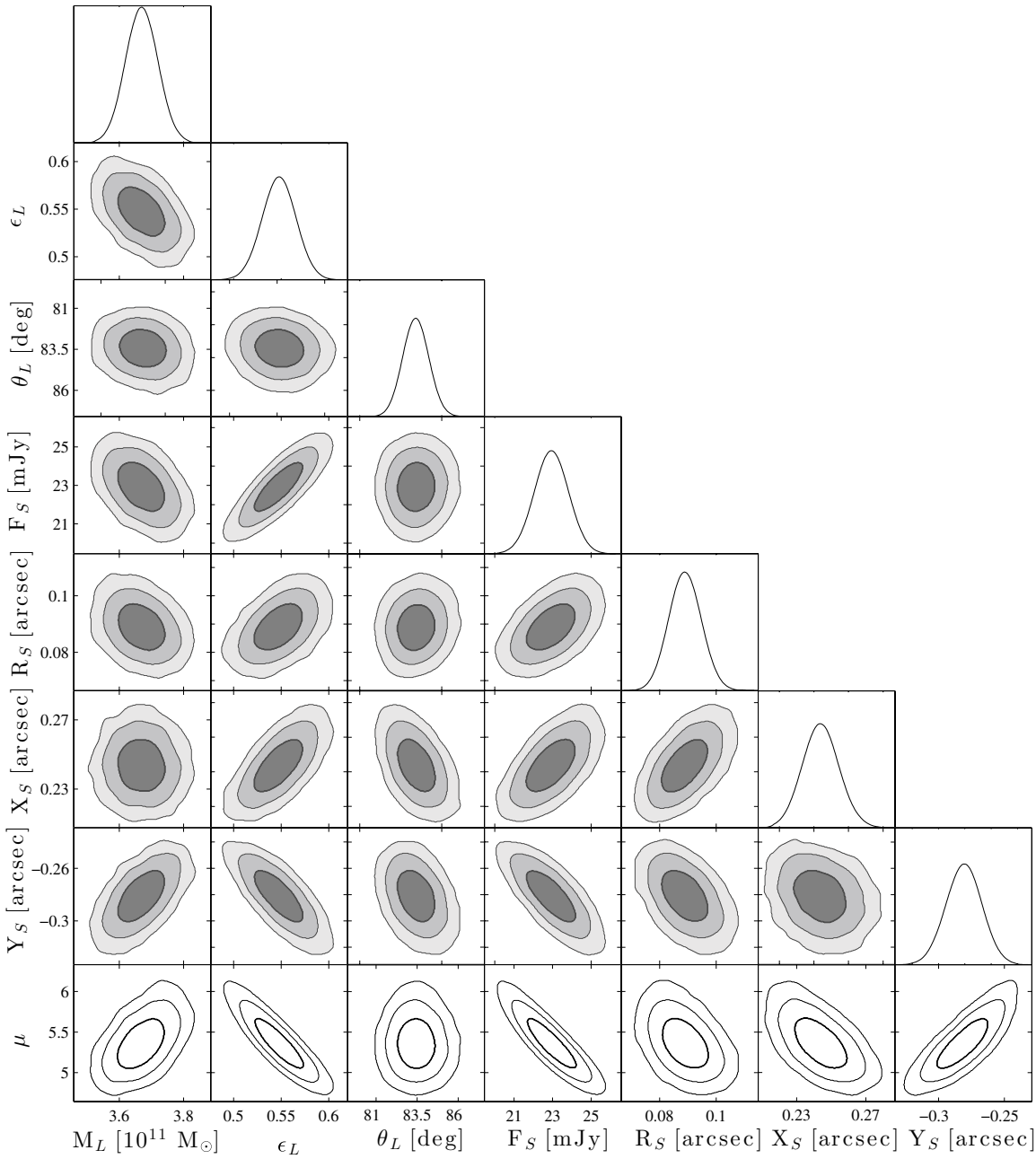

Figure 3. Parameter degeneracy plot for SPT0346-52, a representative example of the model uncertainties. Some nuisance parameters are not shown. Marginalized distributions for each parameter along the bottom axis are shown as histograms on the diagonal. The bottom row shows correlations between μ, which is derived from the model and not a fit parameter, and the model parameters. The contours show the 1σ, 2σ, and 3σ confidence regions.

differencing visibilities that are adjacent in time for the same baseline/polarization/IF, which has the effect of removing all sky signal. This gives results that are identical to those found by scaling the visibility noise to obtain a reduced χ^2 of unity for the best-fit models. We explore the model parameter space using a Markov Chain Monte Carlo (MCMC) method with Metropolis–Hastings sampling. An example of the parameter degeneracies in these fits is shown in Figure 3.

An additional complication of the modeling procedure is the presence of uncorrected antenna-based phase errors in the data. Observations of test sources, quasars with positions referenced to the International Celestial Reference Frame (ICRF), show significant residual phase errors after the primary phase calibration step. For simple source structures, self-calibration using CLEAN components as input for the phase correction is a standard procedure to improve image fidelity (e.g., Taylor et al. 1999). However, in this application, it would add significant complication to model the clean/self-cal process as part of the fitting, and leaving the phase errors uncorrected can significantly bias the model parameters because of the strong sensitivity to image flux ratios in the model. We have therefore developed a procedure to determine the self-cal phases as part of the model fitting. We optimize the χ^2 for each step in the Markov chain by adjusting the $N-1$ antenna phases. We find that the resulting phases vary little over the chain and closely resemble those found for nearby point sources added to the tracks to test the calibration and astrometry, giving us confidence in this method. Additional details of the method and simulations of its effectiveness are provided in the Appendix.

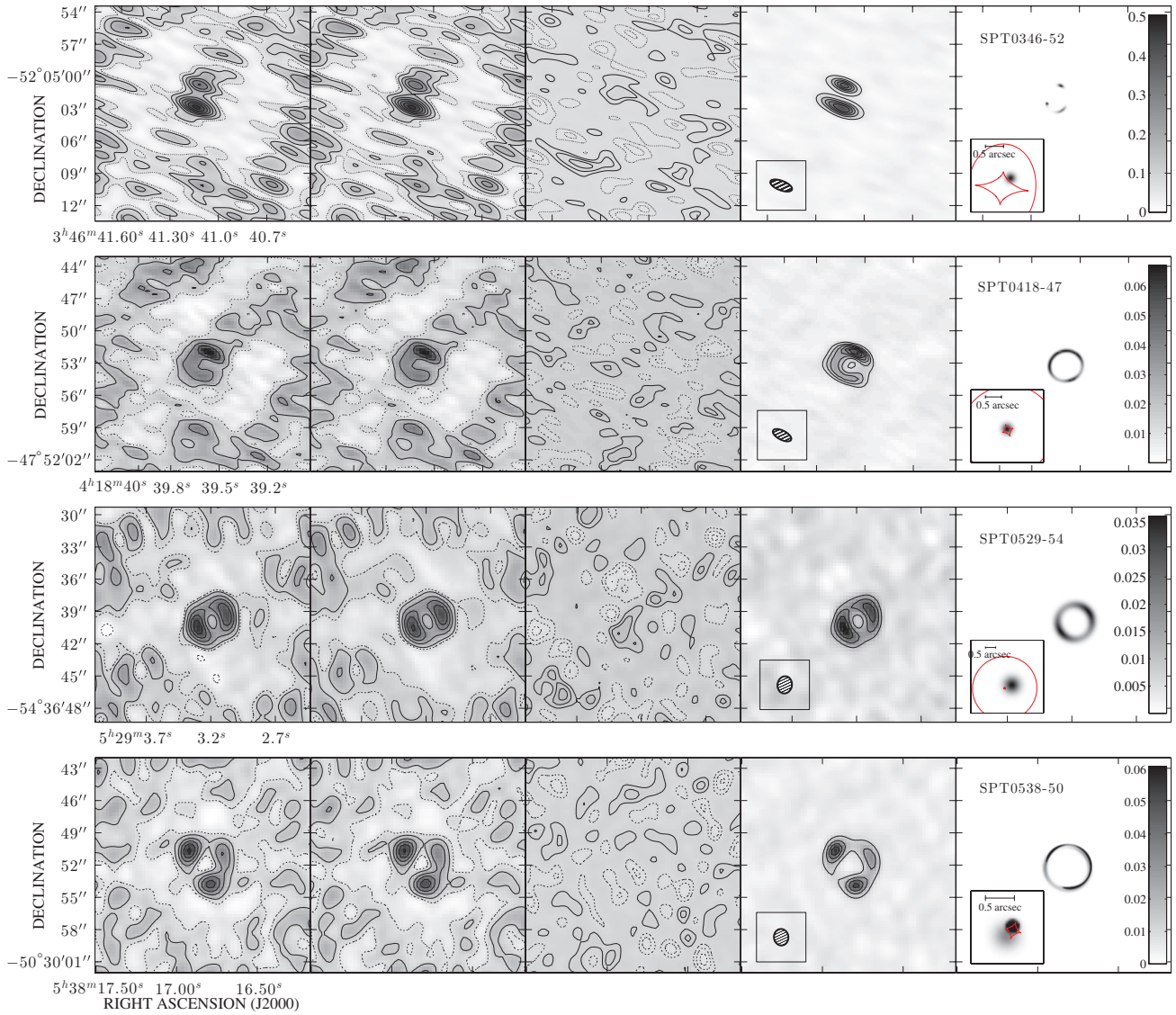

Figure 4. Modeling of the observed submillimeter emission. In each row, the panels from left to right are the "dirty" image, model dirty image, residuals after subtraction, CLEANed image, and fully resolved lens model. Contours in the left two columns start at ±3 times the rms noise in the residual map (third column) and increase in steps of 10 times the rms noise, except in the second row, where they increase in steps of 5 times the rms noise. Contours in the residuals are ±1, 2, etc., times the rms noise, which is (top to bottom) 1.5, 1.7, 1.0, and 1.0 mJy. The contours in the CLEANed images start at 5σ and increase in levels of 10σ for the top and bottom rows and 5σ in the two middle rows. The apparently high significance structure in the dirty maps away from the source is due to the sidelobes of the synthesized (or "dirty") beam, and should therefore be reproduced by the model in the second panel. The insets in the last panels show a magnified view of the positions of the emission in the source plane (grayscale) relative to the lensing caustics (red). In the source model for SPT0538-50, the grayscale is truncated at 10% of the peak intensity to make the second source component visible. The intensity scale for the right panel, in Jy arcsec^{-2}, is given by the colorbar in each figure.

(A color version of this figure is available in the online journal.)

The model parameter space is complex, with the possibility of multiple isolated minima separated by high barriers in χ^2. To decrease the possibility of missing important minima in the posterior, we search the space more broadly by "tempering," which is similar to the simulated annealing method (e.g., Press et al. 2007). A control parameter, T (the analog of temperature), is introduced to flatten the posterior surface and to make the minima more accessible. This is achieved by raising the posterior to the power $1/T$ (with $T > 1$).

4. DISCUSSION

A primary goal of this work is to determine the lensing configuration for bright SPT starburst galaxies and derive the total magnification. Using a simple multi-component source model and a range of lensing geometries, Hezaveh et al. (2012) showed that differential magnification of a DSFG can distort the SED in unpredictable ways by differentially lensing different source plane regions (see also Serjeant 2012 for a similar effect concerning molecular line ratios). A lens model is therefore essential if we wish to correctly interpret observations of these targets and place them in context with existing samples of unlensed starbursts. In principle, spatially resolved imaging of each molecular line is required to map that particular line to the source plane, however, a single lens model based on continuum imaging, combined with physically motivated models for the relative filling factors of the emitting regions in other bands or molecular lines, can be used to place limits on the differential magnification between components.

Models for the four sources are shown in the rightmost panels of Figure 4. Key parameters of the models are reported in

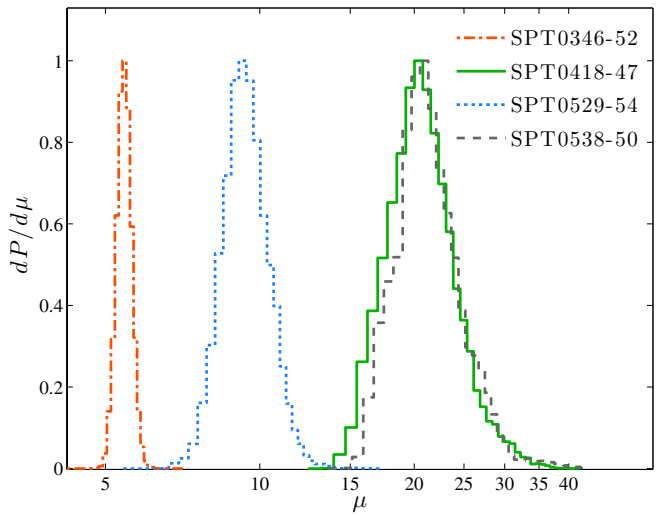

Figure 5. The source magnification distributions derived from the lens models. In the case of SPT0538-50, the total magnification of the two source-plane components is shown.

(A color version of this figure is available in the online journal.)

Table 1. The lens models permit the calculation of some intrinsic properties of the lensed galaxies by simply dividing the observed properties by the magnification. The four sources presented here were detected with 1.4 mm flux densities ranging from 30 to 45 mJy. By correcting for the lensing magnification (Figure 5), we find that the intrinsic 1.4 mm and 860 μm fluxes of these sources vary by a factor of several. The 860 μm fluxes span the range for sources identified in blank field surveys with SCUBA (e.g., Greve et al. 2004; Coppin et al. 2006; Scott et al. 2008; Weiß et al. 2009), suggesting that even without the lensing boost, the galaxies presented in this work would still be identified as luminous starbursts. The far-IR luminosities are even more widely varying, though always in the ultra luminous infrared galaxy (ULIRG) class, indicating star formation rates of several hundred to several thousand $M_\odot$ yr^{-1}.

The intrinsic sizes of the source-plane emission regions ($R_{1/2}$ in Table 1, the half-width at half-maximum for the Gaussian model components) range from 0.5 to 2.4 kpc. This is at the lower range of the sizes generally inferred for starbursts from a variety of observables (e.g., Bothwell et al. 2010; Rujopakarn et al. 2011; Daddi et al. 2010; Tacconi et al. 2006, 2010 and references therein), including synchrotron emission (Chapman et al. 2004; Biggs & Ivison 2008), low-J (Ivison et al. 2011), and even higher-J (e.g., Tacconi et al. 2006) CO measurements. However, the selection of strongly lensed galaxies can result in a biased distribution of intrinsic source size, as noted by Hezaveh et al. (2012).

Some comments on the individual sources:

SPT0346-52. This source has the lowest magnification of the set (5.4 $\pm$ 0.2), and being the brightest of the four targets in apparent $S_{1.4\,\mathrm{mm}}$, it is by far the most luminous after correction for magnification. Unlensed, with a flux density of 26 mJy, it would be among the 860 μm-brightest high-redshift galaxies known. Given the source size, the flux (luminosity per area) is $2.4 \times 10^{13}\ L_\odot$ kpc^{-2}, implying a star-formation rate of 4200 $M_\odot$ yr^{-1} kpc^{-2} assuming a standard conversion for star-bursting galaxies (Kennicutt 1998). This is remarkably high, 50$\times$ higher than the average value found in marginally resolved starbursts by Tacconi et al. (2006) and a factor of several higher than observed for individual giant molecular clouds in the highly magnified source SMM J2135-0102 (Swinbank et al. 2011). The flux is comparable to the Eddington limit (Thompson et al. 2005), and the degeneracy between μ and R_S (shown in Figure 3) is such that larger magnification decreases R_S and further increases the flux.

Thompson et al. (2005) noted that such fluxes are relatively common among low-redshift ULIRGs, which are generally more compact than high-redshift galaxies of similar luminosity, suggestive of a self-regulating process. Because we find the luminosity of SPT0346-52 to arise in a very compact region, its mode of star formation may be more similar to lower-redshift ULIRGs than to most other high-redshift starbursts, despite being at $z = 5.7$. Walter et al. (2009) found a similar star formation density over a region of similar size in a $z = 6.4$ quasar, so this is not unprecedented in the early universe. The optical spectrum of the lens does not show any lines or features that result in a robust redshift for the lens. However, the only lens modeling parameter that is degenerate with the redshifts is the lens mass. The mass of this lens is reported assuming $z = 0.8$ for the lens.

SPT0418-47 and *SPT0529-54*. These sources should present nearly complete Einstein rings at higher resolution. In the case of SPT0418-47, this is due to the excellent alignment of source and tangential caustic. SPT0529-54 is the most extended source in this sample and its large size compared to the caustic fills the ring effectively. In both cases, the luminosities, submillimeter fluxes, and source sizes are very comparable to those

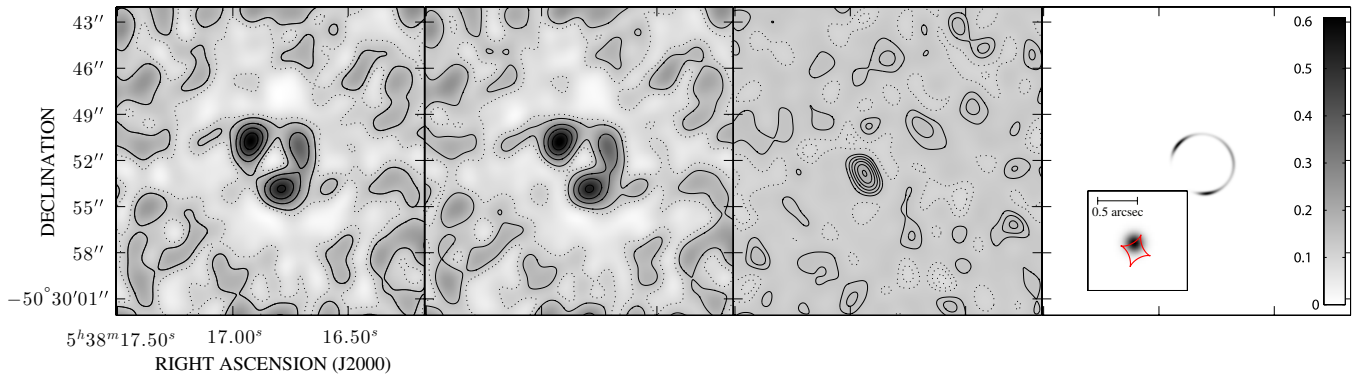

Figure 6. The best fit lens model for SPT0538-50 using a single source component, for comparison with Figure 4. From left to right are the "dirty" image, the model dirty image, the difference between data and model, and the full-resolution source model. Contours in the two panels on the left start at ± 2 times the rms noise in the residual map (σ), increasing in steps of 10σ, while contours in the third panel increase in steps of $\pm 1\sigma$. The peak in the residual map has a significance of $>5\sigma$. As shown in Figure 4, a second source component completely eliminates this high peak and has a significance $>10\sigma$ in the visibility space.

(A color version of this figure is available in the online journal.)

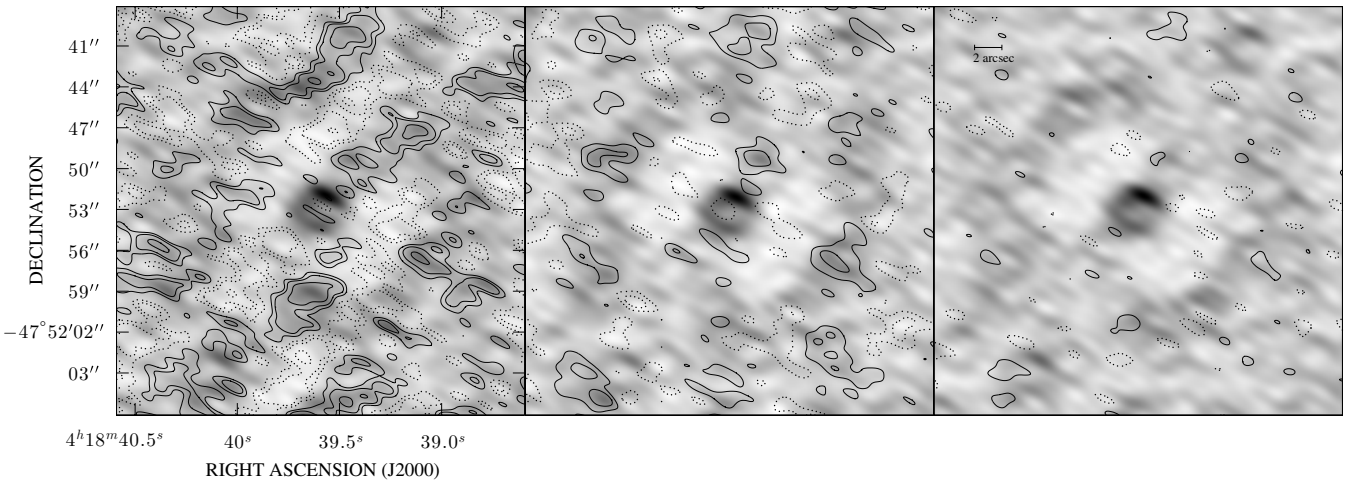

Figure 7. A comparison of image residuals for three different corrections to the antenna phases. The dirty image of SPT0418-47 is shown in grayscale beneath each panel. Contours show the image residuals after the source model is subtracted from the dirty image. Left: residual structure after the model that fits the raw data (no self-calibration) best is subtracted from the data. Middle: the same, but for data calibrated using a CLEAN-based self-calibration. Right: the same, but for data calibrated using the procedure described in this work. The presence of residual structure away from the source, with no corresponding residual at the source position, is a clear sign of imperfectly corrected phase in the left two panels.

observed in other samples of distant starburst galaxies (e.g., Rujopakarn et al. 2011). The posterior of the model parameters for SPT0529-54 show two separate peaks in the lens and source positions, but the magnifications of both models are similar. The extended array data on this source can possibly break this degeneracy.

SPT0538-50. The large angular size of this ring suggests a massive lens, with the models indicating that the lens has a projected mass of nearly $10^{12}\ M_{\odot}$ within a radius of 10 kpc. Close alignment between the compact source (labeled component "A" in Table 1) and caustic again leads to a large magnification. A single-component source does not provide an adequate fit, leaving a significant residual structure to the south east of the lens center (Figure 6). A far better match to the data is the model shown in Figure 4 (bottom), which includes a second source component (labeled component "B" in Table 1) offset from and much more extended than the first, and representing 30% of the total source-plane luminosity.

5. CONCLUSION

We have used ALMA to image the submillimeter emission from four DSFGs discovered by the SPT. We find that these objects resolve into ring-like structures expected from gravitational lensing, a picture confirmed by the redshift information we have for the submillimeter emission and NIR counterparts. We present a visibility modeling procedure to fit gravitational lens models to these data and simultaneously correct the unknown phase errors of the antennas introduced by, e.g., imperfect antenna positions. From this technique, we are able to correct for the magnification of the sources presented in this work and derive intrinsic properties, finding the galaxies to be typical high-redshift, DSFGs. The sensitivity of ALMA permits these lens models to be constrained in short observations. Longer observations of lensed starbursts in future cycles will therefore enable studies of ISM structure and lower luminosity molecular lines that are otherwise impossible to observe in unlensed systems.

The SPT is supported by the National Science Foundation through grant ANT-0638937, with partial support through PHY-1125897, the Kavli Foundation, and the Gordon and Betty Moore Foundation. This paper makes use of the following ALMA data: ADS/JAO.ALMA #2011.0.00957.S and #2011.0.00958.S. ALMA is a partnership of ESO (representing its member states), NSF (USA) and NINS (Japan), together with NRC (Canada) and NSC and ASIAA (Taiwan), in cooperation with the Republic of Chile. The Joint ALMA Observatory is operated by ESO, AUI/NRAO and NAOJ. The National Radio Astronomy Observatory is a facility of the National Science Foundation operated under cooperative agreement by Associated Universities, Inc. Partial support for this work was provided by NASA through grant HST-GO-12659 from the Space Telescope Science Institute and an award for *Herschel* analysis issued by JPL/Caltech for OT2_jvieira_5. Work at McGill is supported by NSERC, the CRC program, and CIfAR. Y.D.H. acknowledges the support of FQRNT through International Training Program and Doctoral Research scholarships. T.R.G. acknowledges support from the Science and Technologies Facilities Council.

APPENDIX

A.1. Lens Model Self-Calibration

Interferometric phase calibration procedures generally leave some residual phase errors due to imperfect baseline solutions, uncompensated atmospheric delays, or other effects. The magnitude of these errors depends on many factors, such as calibration interval and calibrator-source separation, and their importance depends on the signal to noise ratio in the data and the complexity of the imaging task. In the present application, small phase errors can redistribute flux between lensed images, and without properly accounting for such effects in our lens modeling, the derived model parameter distributions may be significantly in error.

A standard procedure to correct antenna-based phase errors is self-calibration. Using a source model derived from images of the corrupted visibilities, phase corrections are derived, the source is re-imaged, and another iteration can be made using a new source model produced from the phase-corrected visibilities. For our present purposes, the most significant disadvantage of this phase correction scheme is that the uncertainties associated with the source model against which the data are

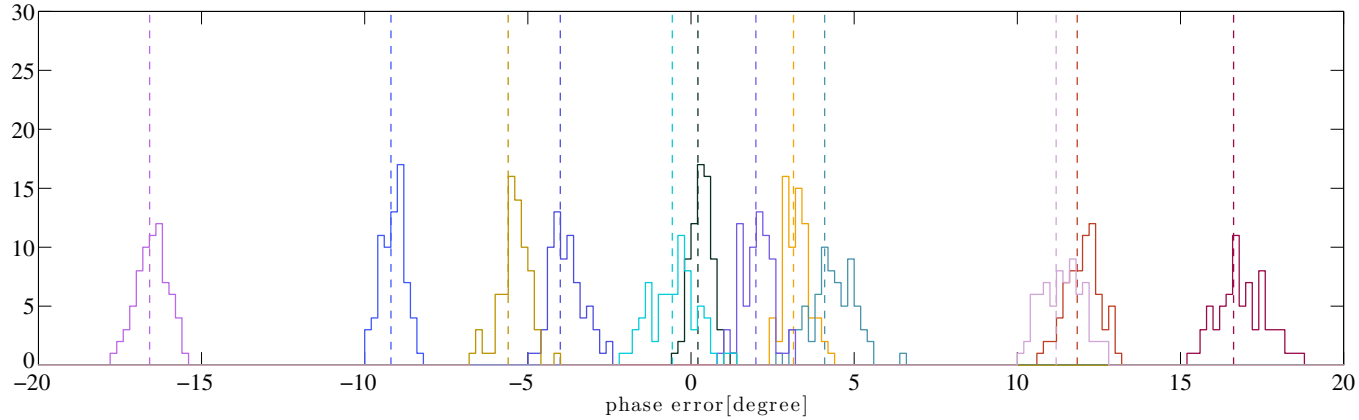

Figure 8. Antenna phase errors recovered in 70 simulated observations of a lens model with different noise realizations. Phase errors were introduced to the antennas, with values indicated by the vertical dashed lines. The histograms show the phase values recovered in fits to the simulated visibilities following the technique outlined here.

(A color version of this figure is available in the online journal.)

self-calibrated are not included in the lens modeling, and any structural errors introduced by noise or phase errors may become a permanent part of the lens model. Here, we propose a method to incorporate the phase correction into the lens modeling procedure, using the lensed structure as the source model for self calibration.

To implement this self calibration technique, we use a perturbative approach in which we assume that the current data is equal to the model plus an antenna based phase corruption. We can write the expression for χ^2 for the visibility phases between the data and model as

$$\chi^2 = \left[\delta\Phi_i + \delta\phi_k \frac{\partial\Phi_i}{\partial\phi_k}\right] C^{-1} \left[\delta\Phi_i + \frac{\partial\Phi_i}{\partial\phi_k}\delta\phi_k\right], \qquad \text{(A1)}$$

where Φ_i is the phase of the i'th visibility, $\delta\Phi_i$ is the phase difference between the model and the data, and $\delta\phi_k$ is the phase delay in the k'th antenna. $\partial\Phi_i/\partial\phi_k$ is a Jacobian matrix containing the gradients of the observed visibilities with respect to changes in antenna phases. For N antennas and M visibilities, $\partial\Phi/\partial\phi$ is an $N \times M$ matrix whose ik'th element is 1 if the first antenna of i'th visibility is k, -1 if the second antenna of i'th visibility is k, and zero otherwise. C is a diagonal covariance matrix whose nonzero elements are approximately $(\sigma_{xy}/|V|)^2$, where σ_{xy} is the rms error on the real or imaginary part of each visibility and $|V|$ is the visibility amplitude. Note that this approximation to the covariance matrix is only valid in the limit of high signal-to-noise data (Wrobel & Walker 1999).

To minimize χ^2, we set its derivative with respect to antenna phases to zero ($\partial\chi^2/\partial\phi_i = 0$). This allows us to write the antenna phase offsets as

$$\delta\phi_l = -(F^{-1})_{lk} \frac{\partial\Phi}{\partial\phi} (C^{-1})_{ji}\ \delta\Phi_i, \qquad \text{(A2)}$$

where F is the Fisher matrix calculated as

$$F_{ij} = \frac{\partial\Phi_k}{\partial\phi_i}(C^{-1})_{kl}\frac{\partial\Phi_l}{\partial\phi_j}. \qquad \text{(A3)}$$

At every iteration of the MCMC code, the value of χ^2 is minimized for the postulated model by deriving calibration phases using Equation (A2). The resulting χ^2 is used to evaluate the likelihood and determine the next link in the chain,

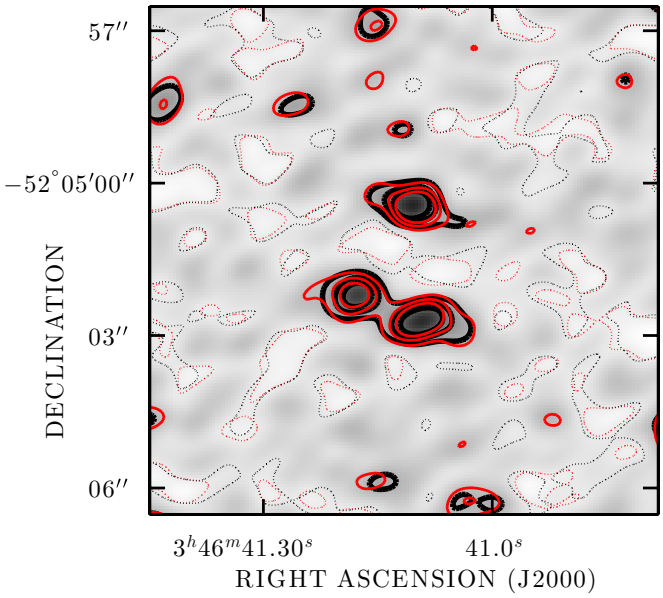

Figure 9. A comparison of the model proposed for SPT0346-52 from the low-resolution observations presented above and the higher-resolution observations obtained after submission. The "dirty" image of the extended configuration observations are shown in grayscale and black contours. The red contours are the predicted appearance given the model of Figure 4 and the uv sampling of the new data. Contours are drawn at -5 (dashed) and 20, 40, and 60 (solid) times the rms noise.

(A color version of this figure is available in the online journal.)

thereby incorporating the uncertain phase correction in the parameter exploration. In the limit of an intrinsically Gaussian distribution for these phase parameters, this is equivalent to marginalizing over the phases. In Figure 7, we compare the results of this procedure with the standard self-calibration based on CLEAN components, and the raw data. The improvement in source subtraction is significant, even compared to the standard CLEAN procedure.

A second test of the simultaneous fitting of the lensed emission and antenna phases is shown in Figure 8. Simulated observations of a typical lens model were created with realistic noise levels, and antenna phase errors were added to these visibilities. The MCMC fitting algorithm was applied to these multiple realizations of the same source to verify that the antenna

phase errors are recovered. The excellent agreement between input and recovered phase demonstrates that the simultaneous fitting of the lens model and antenna phases does not bias the antenna phase measurement, despite the complicated source structure of the lens models.

A.2. High Resolution Observations of Spt0346-52

The models in Figure 4 were derived using the compact configuration data that were available at the time of submission. Higher resolution data were delivered later, and permit a direct comparison of the model based on the low-resolution data with the higher resolution observations of SPT0346-52. Figure 9 shows the predictions of the best fit model (from fitting to the compact data, presented earlier in this work) for the uv-coverage of the extended data (red contours). The black contours show the extended data. The contours demonstrate a high degree of agreement between the predictions and the new observations. A lens model for the extended configuration data shows a consistent model, resulting in magnification (from modeling the extended data alone) of 5.26 ± 0.12 in agreement with the magnification derived from the compact data.

REFERENCES

Appenzeller, I., Fricke, K., Fürtig, W., et al. 1998, Msngr, 94, 1
Barger, A. J., Cowie, L. L., Sanders, D. B., et al. 1998, Natur, 394, 248
Biggs, A. D., & Ivison, R. J. 2008, MNRAS, 385, 893
Blain, A. W. 1996, MNRAS, 283, 1340
Blundell, R. 2004, in Proc. 15th International Symposium on Space Terahertz Technology, ed. G. Narayanan (Northampton, MA: Univ. of Massachusetts), 3
Bothwell, M. S., Chapman, S. C., Tacconi, L., et al. 2010, MNRAS, 405, 219
Bussmann, R. S., Gurwell, M. A., Fu, H., et al. 2012, ApJ, 756, 134
Carlstrom, J. E., Ade, P. A. R., Aird, K. A., et al. 2011, PASP, 123, 568
Chapman, S. C., Blain, A. W., Smail, I., & Ivison, R. J. 2005, ApJ, 622, 772
Chapman, S. C., Smail, I., Windhorst, R., Muxlow, T., & Ivison, R. J. 2004, ApJ, 611, 732
Coppin, K., Chapin, E. L., Mortier, A. M. J., et al. 2006, MNRAS, 372, 1621
Cornwell, T., Braun, R., & Briggs, D. S. 1999, in ASP Conf. Ser. 180, Synthesis Imaging in Radio Astronomy II, ed. G. B. Taylor, C. L. Carilli, & R. A. Perley (San Francisco, CA: ASP), 151
Daddi, E., Bournaud, F., Walter, F., et al. 2010, ApJ, 713, 686
Depoy, D. L., Atwood, B., Byard, P. L., Frogel, J., & O'Brien, T. P. 1993, Proc. SPIE, 1946, 667
Dole, H., Lagache, G., Puget, J.-L., et al. 2006, A&A, 451, 417
Fixsen, D. J., Dwek, E., Mather, J. C., Bennett, C. L., & Shafer, R. A. 1998, ApJ, 508, 123
Fu, H., Jullo, E., Cooray, A., et al. 2012, ApJ, 753, 134
Greve, T. R., Ivison, R. J., Bertoldi, F., et al. 2004, MNRAS, 354, 779
Greve, T. R., Vieira, J. D., Weiß, A., et al. 2012, ApJ, 756, 101
Hauser, M. G., Arendt, R. G., Kelsall, T., et al. 1998, ApJ, 508, 25
Hezaveh, Y. D., & Holder, G. P. 2011, ApJ, 734, 52
Hezaveh, Y. D., Marrone, D. P., & Holder, G. P. 2012, arXiv:1203.3267
Hills, R. E., Kurz, R. J., & Peck, A. B. 2010, Proc. SPIE, 7733, 773317
Ho, P. T. P., Moran, J. M., & Lo, K. Y. 2004, ApJL, 616, L1
Hughes, D. H., Serjeant, S., Dunlop, J., et al. 1998, Natur, 394, 241
Ivison, R. J., Papadopoulos, P. P., Smail, I., et al. 2011, MNRAS, 412, 1913
Kennicutt, R. C., Jr. 1998, ARA&A, 36, 189
Kneib, J.-P., van der Werf, P. P., Kraiberg Knudsen, K., et al. 2004, MNRAS, 349, 1211
Komatsu, E., Smith, K. M., Dunkley, J., et al. 2011, ApJS, 192, 18
Koopmans, L. V. E., Bolton, A., Treu, T., et al. 2009, ApJL, 703, L51
Koopmans, L. V. E., Treu, T., Bolton, A. S., Burles, S., & Moustakas, L. A. 2006, ApJ, 649, 599
Lagache, G., Puget, J.-L., & Dole, H. 2005, ARA&A, 43, 727
Ma, C., Arias, E. F., Eubanks, T. M., et al. 1998, AJ, 116, 516
McMullin, J. P., Waters, B., Schiebel, D., Young, W., & Golap, K. 2007, in ASP Conf. Ser. 376, Astronomical Data Analysis Software and Systems XVI, ed. R. A. Shaw, F. Hill, & D. J. Bell (San Francisco, CA: ASP), 127
Moorwood, A., Cuby, J.-G., Biereichel, P., et al. 1998, Msngr, 94, 7
Negrello, M., Hopwood, R., De Zotti, G., et al. 2010, Sci, 330, 800
Negrello, M., Perrotta, F., González-Nuevo, J., et al. 2007, MNRAS, 377, 1557
Petry, D., & the CASA Development Team 2012, in ASP Conf. Ser., Vol. 461, Astronomical Data Analysis Software and Systems XXI, ed. P. Ballester, D. Egret, & N. P. F. Lorente (San Francisco, CA: ASP), 849
Press, W. H., Teukolsky, S. A., Vetterling, W. T., & Flannery, B. P. 2007, Numerical Recipes: The Art of Scientific Computing (3rd ed.; New York: Cambridge Univ. Press)
Puget, J.-L., Abergel, A., Bernard, J.-P., et al. 1996, A&A, 308, L5
Riechers, D. A., Cooray, A., Omont, A., et al. 2011, ApJL, 733, L12
Rujopakarn, W., Rieke, G. H., Eisenstein, D. J., & Juneau, S. 2011, ApJ, 726, 93
Scott, K. S., Austermann, J. E., Perera, T. A., et al. 2008, MNRAS, 385, 2225
Serjeant, S. 2012, MNRAS, 424, 2429
Siringo, G., Kreysa, E., Kovács, A., et al. 2009, A&A, 497, 945
Smail, I., Ivison, R. J., & Blain, A. W. 1997, ApJL, 490, L5
Swinbank, A. M., Papadopoulos, P. P., Cox, P., et al. 2011, ApJ, 742, 11
Swinbank, A. M., Smail, I., Longmore, S., et al. 2010, Natur, 464, 733
Tacconi, L. J., Genzel, R., Neri, R., et al. 2010, Natur, 463, 781
Tacconi, L. J., Neri, R., Chapman, S. C., et al. 2006, ApJ, 640, 228
Taylor, G. B., Carilli, C. L., & Perley, R. A. (ed.) 1999, ASP Conf. Ser. 180, Synthesis Imaging in Radio Astronomy II (San Francisco, CA: ASP)
Thompson, T. A., Quataert, E., & Murray, N. 2005, ApJ, 630, 167
Treu, T., & Koopmans, L. V. E. 2004, ApJ, 611, 739
Vernet, J., Dekker, H., D'Odorico, S., et al. 2011, A&A, 536, A105
Vieira, J. D., Crawford, T. M., Switzer, E. R., et al. 2010, ApJ, 719, 763
Vieira, J. D., et al. 2013, Natur, 495, 344
Walter, F., Riechers, D., Cox, P., et al. 2009, Natur, 457, 699
Wardlow, J. L., Cooray, A., De Bernardis, F., et al. 2013, ApJ, 762, 59
Weiß, A., De Breuck, C., Marrone, D. P., et al. 2013, ApJ, 767, 88
Weiß, A., Kovács, A., Coppin, K., et al. 2009, ApJ, 707, 1201
Wrobel, J. M., & Walker, R. C. 1999, in ASP Conf. Ser. 180, Synthesis Imaging in Radio Astronomy II, ed. G. B. Taylor, C. L. Carilli, & R. A. Perley (San Francisco, CA: ASP), 171
Wucknitz, O., Biggs, A. D., & Browne, I. W. A. 2004, MNRAS, 349, 14